Unraveling the properties of sharply defined submicron scale FeCu and FePd magnetic structures fabricated by electrodeposition onto electron-beam-lithographed substrates

Evangelia Dislaki[a,*], Matteo Cialone[b], Federica Celegato[b], Paola Rizzi[c], Paola Tiberto[b,*], Simone Vadilonga[d], Daniel Többens[d], Jordi Sort,[a,e,*], Eva Pellicer[a]

[a] Departament de Física, Universitat Autònoma de Barcelona, 08193 Bellaterra, Spain

[b] INRIM, Strada delle Cacce 91, 10135 Torino, Italy

[c] Dipartimento di Chimica, Università di Torino, Via Giuria 7, 10125 Torino, Italy

[d] Helmholtz-Zentrum Berlin für Materialen und Energie GmbH, Albert-Einstein-Str. 15, D-12489 Berlin

[e] Departament de Física, Universitat Autònoma de Barcelona, 08193 Bellaterra, Spain

Institució Catalana de Recerca i Estudis Avançats (ICREA), Passeig Lluís Companys 23, 08010 Barcelona, Spain

To whom correspondence should be addressed: evangeliadislaki@gmail.com (E.D.), p.tiberto@inrim.it (P.T.), Jordi.Sort@uab.cat (J.S.)

Abstract

In this work, Fe–X (X=Cu, Pd) submicron-scale structures were electrochemically deposited onto pre-patterned substrates prepared by e-beam lithography. The FeCu and FePd (with reduced Pd content) systems were investigated as attractive candidates for a variety of potential applications in magnetic data storage and biomedicine. Confined growth in the restricted cavities resulted in a nanoscale grain size leading to well-defined geometries with sharp edges and corners and an average height of up to 215 nm. Specifically, nine 100 μm x 100 μm arrays of three selected geometries (cylindrical, rectangular and cruciform) in three different sizes were created. In addition, the total deposition time ranged from 3.5 s (for FeCu) to 200 s (for FePd), i.e. much faster than by traditional physical vapor deposition approaches and was performed at ambient conditions using a low-cost setup. Magnetic force microscopy for the cylindrical and cruciform structures revealed virtually no contrast at zero field, suggesting magnetic curling effects (instead of coherent rotation) during magnetization reversal. These curling effects result in low values of remanent magnetization, which is advantageous in minimizing dipolar interactions between the structures either when they are deposited onto the substrate or eventually dispersed in a liquid (e.g. in biomedical applications, as drug delivery carriers, where particle agglomeration is undesirable).

Keywords: electrodeposition, submicron structures, electron-beam lithography, ferromagnetic

1. Introduction

Since the discovery of giant magnetoresistance and its implementation in magnetic field sensors [1], the field of nanomagnetism has experienced rapid developments in the last decades given the novel properties that have been discovered in the field of spintronics with major implications for data processing and storage [2,3] as well as the highly promising and fascinating functionalities of flexible electronics [4]. The growing trend towards miniaturization faces challenges related to spin wave guidance [5] and the superparamagnetic limit which need to be addressed in a holistic approach that combines several traditional disciplines under the umbrella of nanomagnetism [6]. The vast majority of existing studies have focused on two-dimensional nanomagnetism where single- or multi-layer films and structures are confined to a thickness that leads to monodomain magnetic states in the vertical direction and interesting functionalities are achieved by capitalizing on interfacial effects [7-10]. Nevertheless, new fabrication and characterization techniques enable the expansion of nanomagnetism into three dimensions where unconventional spin textures bring about remarkable new phenomena involving geometry, topology and chirality. Indeed, patterned 3D nanostructures can revolutionize sensing technology, ultrahigh density magnetic recording and the Internet-of-Things while 3D nano-and micro-scale magnetically actuated motors are essential for mechano-biology applications [11].

From a synthesis point of view, electrodeposition is widely used due to its conformal coverage, control of grain size and crystallinity and fast growth rates. When combined with ultra-high-resolution electron-beam lithography, well-defined nano-motifs can be created. The height of the submicron motifs produced by physical vapor deposition (PVD) approaches is typically below 50 nm [7,12,13] and in order to reach an approximate thickness of 200 nm several

successive time-consuming steps including sputter etching can be involved.[14] Contrarily, it is easily possible to achieve a high aspect ratio with electroplating. Nevertheless, existing literature on electrodeposited 3D structures has thus far been focused on arrays of nanowires [15-17].

Herein, submicron FeCu and FePd structures organized in nine 100 μm x 100 μm arrays of three select shapes (disks, stripes and crosses) and of three sizes each have been prepared by electrodeposition onto e-beam lithographed substrates. With respect to the FeCu system, the optimized electrolyte and plating conditions formerly determined for the growth of FeCu films were adapted as necessary for the deposition of Fe-rich miniaturized patterns. Moreover, it was shown that the saturation magnetization and coercivity of electroplated FeCu films can be tuned by a facile adjustment of the Fe content [18]. It was also demonstrated that the coercivity of hierarchically porous FeCu thin films with ultrathin pore walls was successfully reduced up to 25% by an applied voltage uncovering the potential for applications in magnetoelectrically driven devices [19]. Interestingly, Chien et al. reported that, while the magnetic moment of Fe often rapidly declines with alloying due to the magnetic weakness of Fe, it remains nearly constant up to high concentrations of Cu in the FeCu system [20]. The inclusion of Cu can also boost corrosion resistance and confer antibacterial properties [21]. With sustainability presenting an increasing concern on a global scale, Fe and Cu are among the most abundant and low-cost materials with excellent recyclability and are non-toxic to the environment. In the case of the FePd system, the electrolyte composition was directly derived from the work of Konczak et al. [22]. and the plating parameters were tailored towards a particular stoichiometry, namely the $Fe_{70}Pd_{30}$ alloy. At this particular composition, interesting properties both from the magnetic and mechanical point of view can be derived. Indeed, in its martensitic phase, the alloy possesses a ferromagnetic shape memory effect [23,24], which makes it an excellent

candidate for wirelessly actuated mechanical systems or strain sensors [25]. Moreover, FePd is a promising alloy in the field of spintronics where it has recently been used in the field of artificial spin-ice [26] and its ability to stabilize skyrmions at room temperature has been proven by ab-initio calculations [27]. On the other hand, the presence of palladium in the alloy makes it an appealing candidate for hydrogen absorption [28,29] and catalysis [30,31]. Finally, FePd alloys can be easily integrated into biomedical and bioengineering applications, given that biocompatibility assessments have clearly established that many different cell types can spread and proliferate well on FePd single crystal as well as polycrystalline films [32].

Morphological and structural information of the resulting deposits was obtained by scanning electron microscopy (SEM), atomic force microscopy (AFM), transmission electron microscopy (TEM) and X-ray diffraction (XRD) using synchrotron radiation. The structures were very well-resolved and relatively smooth with a thickness ranging between 200-300 nm while plating time was as low as 3.5 s (FeCu) and 200 s (FePd), i.e. much faster than is typically feasible with PVD techniques. Overall composition was initially assessed by energy dispersive X-ray spectroscopy (EDX)/SEM while local elemental maps were obtained by EDX/scanning TEM (STEM) and electron energy loss spectroscopy (EELS). The FeCu structures exhibited a graded composition with a rather homogeneous $Fe_{60}Cu_{40}$ stoichiometry at the center region while the FePd motifs showed an even distribution of the Fe and Pd elements. The magnetic properties were investigated using magnetic force microscopy (MFM) as well as using a vibrating sample magnetometer (VSM) for large single-feature arrays of three selected geometries and dimensions (small- and large-sized disks and medium crosses). The MFM results suggested curling of the magnetization rather than coherent rotation. The combination of the biocompatibility of FePd with the presence of magnetization curling, opens up the possibility for applications in the field of mechanically induced cell destruction as a treatment

for cancer [33]. This mechanism has been proven to be a successful approach using permalloy ($Fe_{80}Ni_{20}$) disks where the application of an alternating magnetic field causes the magnetic disks to oscillate thus compromising membrane integrity and initiating cell death. However, when using non-biocompatible materials such as permalloy, an additional layer of gold as a surface coating is necessary [34].

2. Experimental

2.1 Fabrication details

The lithography patterns were created with a FEI Quanta 3D dual beam FEG which combines a focused ion beam (FIB) with a high-resolution field emission gun scanning electron microscope (FEG-SEM). Silicon/silicon dioxide (Si/SiO_2) substrates were used with a 15 nm Ti adhesion layer and an 80 nm Au seed layer, both deposited by e-beam evaporation. The process was controlled by the nanometer patterning generation system (NPGS) software. The information on the dimensions and positions of the different structures, the sizes of the arrays and their reciprocal position on the sample surface were contained in a computer-aided design (CAD) file managed by the NPGS. The features were designed with sufficient spatial separation so as to avoid the proximity effect. The electron dose was 400 μC cm^{-2} for the smallest-sized feature arrays and 375 μC cm^{-2} for the rest. The operating voltage was 30 KeV. Electrodeposition was carried out in a three-electrode cell connected to a Metrohm / Eco Chemie Autolab PGSTAT302N potentiostat / galvanostat. A Pt wire served as the counter electrode and a double junction Ag|AgCl (E = +0.210V/SHE) electrode (Metrohm AG) with a 3M KCl inner solution and a 1M Na_2SO_4 outer solution was used as a reference.

2.2 Sample preparation and post-process treatments

Prior to lithography, the substrates were cleaned successively with acetone, isopropanol and de-ionized water. The substrates were subsequently spin-coated at 2000 rpm for 1 min with a layer of poly(methyl methacrylate) (PMMA) polymeric resist. This ensured that a homogenous layer of PMMA was formed on top of the conductive substrates. The thickness of the resist was around 300 nm, as measured by ellipsometry. After coating, the PMMA was heat treated for 5 min at 165 °C. Upon completion of the patterning procedure, the PMMA in the exposed regions was removed by placing the samples for 60 s in a 1:3 solution of 4-methyl-2-pentanone with isopropanol, followed by 20 s in isopropanol and, finally, 20 s in de-ionized water. Subsequent to electrodeposition, the samples were placed in acetone for 10 min to remove the remaining PMMA leaving behind the created structures of different geometries attached to the substrate. This was followed by a final rinsing in isopropanol and Milli-Q water.

The TEM lamellae preparation was made on a dual beam Carl Zeiss Neon 40 station equipped with a Schottky FE-SEM and Ga+ ion columns (CANION31, Orsay). The lamellae, about 60nm in thickness, originated from a section of the medium-sized cruciform structures. The region of interest was first covered with a thin Pt layer of approximately 200 nm using e-beam assisted Pt deposition. On top of the thin Pt layer, a thicker Pt layer (≈500 nm) was added by ion-beam assisted Pt deposition. Both Pt layers were used in order to protect the underlying structures from ion beam damage during lamella preparation.

2.3 Electrolytes and plating conditions

The electrolytes were prepared with Millipore Milli-Q water and ACS Reagent grade chemicals purchased from Sigma-Aldrich. For the deposition of the FeCu structures, the solution contained ammonium ferrous sulfate hexahydrate (58.8 g L^{-1}), copper (II) sulfate pentahydrate (0.625 g L^{-1}), sodium gluconate (22.9 g L^{-1}), sodium dodecyl sulfate (0.2 g L^{-1}) and saccharine (0.46 g L^{-1}) (Solution A). The as prepared pH was 4.1 and the temperature was adjusted to 45 °C through use of an external thermostatization jacket. Electrodeposition was carried out in potentiostatic mode at an applied potential of -1.1 V for 3.5 s with magnetic stirring at 300 rpm.

For the electrodeposition of the FePd structures, a reduction of the gap in the standard electrode potentials of Fe and Pd can be achieved through complexation of the Pd^{2+} ions with ammonia [35]. The electrolyte composition consisted of tetraamminepalladium(II) chloride (0.01 M), 5-sulfosalicylic acid dihydrate (0.06 M), iron(III) sulfate heptahydrate (0.05 M) and ammonium sulfate (0.3 M) [19]. Sulfosalicylic acid (SSA) has been proposed in literature as a means to stabilize the Fe-ions and to prevent hydroxide formation and incorporation [36]. In particular, the ratio between the concentration of the Fe^{3+} ions and the SSA was kept at $[Fe^{3+}]$:[SSA] = 1:1.2 and the pH was adjusted to 5 with addition of ammonium hydroxide. To obtain the desired $Fe_{70}Pd_{30}$ alloy composition, deposition was performed potentiostatically at -0.95 V for 200 s at room temperature and without stirring the electrolyte.

2.4 Characterization

The morphology of the patterned structures was observed using a Zeiss MERLIN field emission scanning electron microscope (FE-SEM) and the elemental composition was determined by

EDX at an acceleration voltage of 15 kV. Additional EDX mappings were acquired with a FEI Magellan 400L XHR SEM. Further chemical analysis at nanometer level and elemental mappings as well as study of crystalline structure by selected area electron diffraction (SAED) was conducted with a FEI Tecnai G2 F20 200 kV field emission gun high resolution and analytical TEM/STEM. The crystalline structure of the submicron FeCu and FePd structures was also investigated via XRD using synchrotron radiation at the KMC-2 beamline at the BESSY II facility [37]. Radiation energy was selected as 8048 eV for a wavelength of 1.5406 Å, equivalent to Cu-Kα_1. An area detector with an angular aperture of 12° was used. The sample was mounted on a cradle allowing for movement and rotation of the sample along the x, y and z directions. Moreover, the incidence and reflection angle could be controlled separately. The incidence angle of the beam was 21.5° both in the case of the FeCu and of the FePd sample. Under these conditions, it was possible to limit the beam footprint on the sample surface to an area smaller than 100 μm x 100 μm, enough to achieve the desired lateral resolution to distinguish among the different arrays of structures. For both the FePd and FeCu sample, 6 fine scans of 10 minutes each were recorded for every array. The different patterns were averaged to reduce the noise of the measurement and then analyzed using the Fityk software [38]. Atomic and magnetic force microscopy were performed with a Bruker Multimode V Nanoscope 8 microscope equipped with a fully non-magnetic head and scanner and with an electromagnet capable to apply fields up to 1000 Oe in the sample plane. The tip used for the magnetic characterization was s a commercial Bruker MESP-HR10 cantilever coated with Co/Cr hard magnetic alloy. Both the in-plane and perpendicular coercivity of the tip are on the order of 900 Oe. The magnetic domain evolution was studied at room temperature under application of an in-plane magnetic field with values up to 600 Oe. All the samples were demagnetized along the in-plane direction prior to the MFM characterization. For further magnetic characterization,

samples patterned with a large array of a single geometry and size were fabricated and placed in a vibrating sample magnetometer from LOT-Quantum Design. Hysteresis loops were recorded at room temperature, along the in-plane direction with an applied field range of -20 kOe to 20 kOe.

3. Results and discussion

3.1 Morphology of patterned structures

While existing literature on lithographed patterns mainly focuses on the fabrication of cylindrical arrays [39-42], this work targets more complex geometries. The dimensions of the various motifs are given in **Table 1**. As can be viewed in **Figure 1** and **Figure 2**, the electrodeposited FeCu and FePd arrays of different shapes and dimensions have a well-defined geometry with sharp edges in the case of the medium- and large-sized crosses and stripes thanks to the small grain size achieved by electrodeposition. This is significant considering the submicron dimensions of the structures and, especially, the complex geometry of the cross-shaped motifs which are characterized by several edges and corners separating them into segments along their axes of symmetry. Notably, the FePd structures appear very dense while the FeCu structures display a granular morphology. Differences in surface morphology stem from the different electrolyte formulations and parameters used (see Experimental section). Note that replacement of the copper salt by the palladium salt in the FeCu bath or vice versa in the FePd bath does not work. Importantly, electrodeposition was carried out at a pH of 4.1-5.0, hence avoiding the use of environmentally unfriendly, highly acidic electrolytes.

The average height and roughness of the FeCu and FePd structures, as determined by analysis of the AFM images acquired, are shown in **Table 2** and **Table 3**, respectively. These values are consistent considering that the deposition time was the same (3.5 s and 200 s for FeCu and FePd, respectively) for all structures. Interestingly, the FeCu medium-sized features were generally at the upper range limit for the height, while the larger stripes were the shortest. In the case of the FePd structures, the larger features displayed more roughness due to increased deposition around the edges while the smallest geometries were also the shortest. The occurrence of donut-like structures due to an uneven distribution of the current density in the cavities can occur when electroplating dot arrays [43,44]. In the case of the FeCu and FePd disks, it can be easily observed that the structures are fully plated in the center. This means that current distribution is homogeneous within the cavities, which can be partly due to the beneficial effect imparted by the additives present in the FeCu and FePd electrolytes.

In **Figure 3**, AFM images of the large-sized FeCu and medium-sized FePd structures are shown where the very small grain size is visible. This resulted in the growth of well-resolved geometries despite the narrowness of the cavities especially at the corners. Due to the high aspect ratio of the structures and the dimensions of the AFM/MFM tip used, the convolution between the two gives an inaccurate representation of the structures on the xy plane. This effect is more visible along the fast scan direction (in this case, the y direction). This is especially true as feature size decreases and, consequently, the AFM images of the smallest-sized structures were less reliable for subsequent surface analysis. Therefore, the SEM micrographs offer a direct representation of geometrical aspects while the AFM images act in a complementary manner to further investigate morphology and estimate height and roughness since very accurate measurements can be obtained in the z-axis direction.

3.2 Chemical and structural analysis of structures

For the deposition of the FeCu submicron structures, the optimized plating parameters previously established for the fabrication of Fe-rich FeCu films [18] were utilized. However, in the case of the structures, the very short plating time of 3.5 s into submicron cavities and the use of potentiostatic rather than galvanostatic deposition mode led instead to a Cu-rich composition, namely 20 at% Fe and 80 at% Cu in average. In order to enhance Fe deposition, the Cu salt amount was then halved. Initial elemental analysis by SEM/EDX after this modification of the Cu salt concentration showed an average value of 45 at% Fe and 55 at% Cu which varied slightly for the different arrays. Notably, a compositional gradient can occur when depositing a system with low mutual solubility such as FeCu [45] into cavities of high aspect ratio, and thus the composition determined by SEM/EDX represents only an overall value with no further insights into deposit growth mechanisms. Therefore, a lamella was prepared from a section of the array of the intermediate-size crosses for STEM/EELS characterization and the results of the analysis are shown in **Figure 4a** and **Figure 5**.

The bright-field images of the FeCu lamella, as seen in **Figure 4a**, show a columnar growth with coarse grains. In **Figure 5a**, the indexed SAED pattern collected from a spot in the middle of the lamella displays the typical Debye-Scherrer rings with small bright spots confirming the nanocrystalline nature of the deposited structures. The presence of two phases was detected, namely a body-centered cubic (bcc) and a face-centered cubic (fcc) which correspond to Fe-rich and Cu-rich solid solutions, respectively. The measured interplanar distances indicate phase separation with partial alloying. From the high-resolution (HR) TEM image in **Figure 5b**, we can observe the sharply defined lattice planes with distances of 0.207 nm. This distance corresponds to the bcc (110) planes of Fe with an increase in value due to the incorporation of

Cu atoms into the lattice. In **Figure 5c**, the quantitative STEM/EDX chemical maps, taken vertically starting from the substrate and extending beyond the surface, show a rather uniform distribution of Fe in the middle of the lamella with a sudden decrease at the uppermost section while copper deposition is favored near the top. Compositionally graded materials are utilized in perpendicular magnetic media as a way of achieving a graded anisotropy which leads to a reduction in coercivity, and thus in the field required to record data [46-48]. The advantage of the electrochemical approach herein is the possibility to create a graded composition through a simple and fast process without the need of high vacuum. With respect to oxygen content, O counts were concentrated within the Fe-rich region close to the substrate and in the area above the surface of the lamella. Since it is known that oxides/hydroxides during Fe electrodeposition often form at the working electrode due to local pH changes, the co-presence of Fe and O in regions close to the substrate is thus anticipated. Likewise, passivation of the structures upon standing in air leads to the accumulation of oxygen at the surface of the lamella. These trends were further confirmed by vertical extreme high-resolution (XHR) SEM/EDX line scans where the Fe content was found to be roughly 60 at% along the middle section. Horizontal line scans revealed a rather homogeneous distribution of Fe and Cu (**Figure S1** of the Supporting Information).

The EELS compositional map seen in **Figure 5d**, which was taken at a starting region close to the center and encompassing upper parts of the lamella, displays Fe-rich and Cu-rich areas as well as areas with a mixed composition where partial alloying takes place. It has been well established in literature that the mutual solid solubility of iron and copper is very low in equilibrium conditions despite their similar atomic radii due to the positive enthalpy of mixing, ΔH_{mix} (calculated value of $\Delta H_{mix} \approx +13$ kJ mol^{-1} in the liquid phase) [49], which encourages clustering of the atoms into Fe-rich and Cu-rich groups to reduce the internal energy [50].

A similar analysis was performed for the FePd crosses to study the compositional and structural characteristics originating from the growth in restricted patterns. In comparison, the microstructure was shown to be very fine, as seen in **Figure 4b.** Additionally, as seen by juxtaposing **Figure 5a** with **Figure 6a**, the FePd structures were more nanocrystalline than their FeCu counterparts. EELS elemental mapping (**Figure 6d**) revealed that the Fe and Pd elements are homogeneously distributed, with no evident Fe-rich or Pd-rich regions. Vertical EDX line scans also evinced a uniform elemental distribution (**Figure S2** of the Supporting Information). This is expected given the high miscibility of Fe and Pd [51] for which the enthalpy of mixing is negative (calculated value of $\Delta H_{mix} \approx$ -4 kJ mol^{-1} in the liquid phase) [49]. The reduction in the internal energy of the system is thereby achieved by increasing the number of Fe–Pd bonds [50]. On the other hand, oxygen is detected primarily at the surface of the sample and in the substrate (originating from the SiO_2 layer) thus confirming the metallic nature of the deposits. STEM/EDX quantification resulted in an average composition of 62 at% Fe and 38 at% Pd, indicating a slightly higher Pd content compared to earlier SEM/EDX measurements which revealed an average overall composition of $Fe_{70}Pd_{30}$ with slight variations among the arrays as well as the individual structures. This discrepancy, therefore, could be due to the superior spatial resolution of the STEM/EDX measurement. Analysis of the SAED pattern revealed the presence of a bcc phase and a fcc phase, corresponding to the α-(Fe,Pd) and the disordered γ-(Fe,Pd) solid solutions. The lattice fringes in **Figure 5b** reveal the crystalline nature of the deposits and the interplanar distance, as determined by Reduced Fast Fourier Transformation (RFFT), was 0.22 nm which corresponds to the bcc (110) planes of the α-(Fe,Pd) solid solution.

In the pursuit of uncovering possible microstructural variations dependent on size and geometry, additional characterization by XRD was performed at the BESSY II synchrotron radiation facility for each of the FePd nine 100 μm x 100 μm FeCu and FePd arrays. In **Figure**

7, the synchrotron X-ray diffraction patterns obtained from the FeCu and FePd medium-sized disks are shown. Similar trends were observed among the different geometries (as such the patterns acquired from all of the individual arrays are included in **Figure S3** of the Supporting Information). The reduced intensity of the signal was a combined result of the reduced footprint of the X-ray beam on the sample surface and the percentage of the surface covered by the structures in the area illuminated by the beam (ranging from 6% to 19%). Additionally, given the high Fe content of both the FeCu and FePd structures, a predominant bcc phase was expected. Indeed, it was not possible to discriminate any reflection peaks originating from the fcc Cu and γ-(Fe,Pd) phases of the FeCu and FePd arrays, respectively, which had previously been detected by the SAED analysis. Moreover, the γ-(Fe,Pd) phase was most likely a minority phase well below the detection threshold of the instrument. Here, it is important to mention the different scales in which the two experimental techniques work. Indeed, with SAED, the diffraction data are generated from a very narrow spot (in the order of hundreds of nanometers) in a well-defined region of a single structure. Contrarily, the XRD experiment performed at the synchrotron targeted an entire array averaging the signal over all the structures.

To determine the angular position of the reflection peaks, they were fitted using a pseudo-Voigt function. Before performing the fit, a cubic spline was used as a baseline to remove the background. The 2θ values were obtained through the fit, while the d-spacings and lattice constants were calculated using Bragg's law. Only the results related to the FeCu and FePd crosses are included in **Table 4** and **Table 5**, respectively (supplementary data for the disks and stripes can be found in **Tables S1-S4** of the Supporting Information).

In the case of the FeCu crosses, if we compare the tabulated angular position of the bcc (110) planes corresponding to pure α-Fe (2θ = 44.67°) with the ones obtained from the measurements

($44.05^o < 2\theta < 44.50^o$), we can observe a shift towards lower angles. This is due to an increase in the length of the crystal lattice parameter driven by the dissolution of Cu into the bcc Fe phase. Indeed, at nano dimensions, surfaces and interfaces have been shown to bring about a modulation of the solubility gap as observed in the case of systems such as Au-Si, Ge-Si and Al-Cu [52].

The investigation of the FePd structures revealed the presence of the bcc (110) reflection of the α-(Fe,Pd) solid solution at $43.05^o < 2\theta < 43.33^o$, for all geometries and sizes. The crystal lattice decreases with increasing dimensions pointing towards a modulation of the solubility of Pd into the α-Fe phase.

3.3 Magnetic characterization of the FeCu and FePd motifs

In consideration of the stoichiometries of the FeCu structures as determined by STEM/EDX elemental analysis, i.e. 60 at% Fe and 40 at% Cu, it should be mentioned that the value of saturation magnetization for a $Fe_{39}Cu_{61}$ film was previously measured at approximately 83.7 emu g^{-1} and for a $Fe_{73}Cu_{27}$ film it was 152.5 emu g^{-1} [18]. Consequently, despite the relatively high overall Cu content of these motifs, a clear magnetic response is expected. In order to study the magnetization reversal of the fabricated structures, each of the nine arrays was exposed to an in-plane static magnetic field of 600 Oe and images were recorded by MFM. Additional images were taken at remanence. The field was then applied in the opposite direction and the same process was repeated. By comparison, when the field is removed, the images become rather featureless thus suggesting curling of the magnetization instead of coherent rotation [53,54]. The MFM images taken at a static field show a single domain state with reverse polarity. Representative images for the medium disks and crosses, where dipolar contrast is

evident and opposite upon field reversal, are seen in **Figure 8**. In the case of the crosses, however, a different behavior can be discerned along the long and short axis. Indeed, along the long axis the dipolar contrast is clearly reversed once the magnetic field is reversed. Nevertheless, the change in contrast along the short axis is less pronounced. This behavior suggests that the shape anisotropy promotes orientation of the magnetization along the axis that is parallel to the direction of the magnetic field and plays a fundamental role on the magnetization reversal mechanism.

Finally, since the positioning of different geometries on the same substrate did not allow acquisition of hysteresis loops of each individual array, three substrates with large single-feature arrays were also prepared. Specifically, a 6x6 and a 12x12 pattern were created by repetition of the small- and large-sized disk array, respectively, as well as a 16x16 duplication of the medium cross array. In this way, two geometries as well as three different feature sizes could be assessed. The number of duplications for each pattern was selected so as to ensure an adequate signal by VSM. The hysteresis loops recorded at room temperature corresponding to the single feature arrays, are shown in **Figure 9**. The strong diamagnetic background originating from the substrate has been subtracted. The measured coercivities were approximately 81 Oe, 114 Oe and 174 Oe for the large disks, small disks and medium crosses, respectively. It can also be observed that saturation is reached at an applied field of more than 1000 Oe. At 600 Oe, the maximum field applied by MFM, the structures could not reach saturation and this held especially true for the large-sized features. However, it was not possible to further increase the applied field without inducing a reversal in the magnetization of the MFM tip. Importantly, at maximum applied field, no interaction between the magnetization of the structures and the magnetization of the tip was observed.

Conversely, for the FePd structures, a maximum field of 400 Oe was adequate to saturate the structures in the in-plane direction. Interestingly, when higher fields up to 600 Oe were applied, an interference between the magnetic moment of the tip and the stray field of the structures was observed. Taking this into consideration, we can infer that the FePd structures are magnetically softer than their FeCu counterparts. As can be observed in **Figure 10**, upon reversal of the magnetic field, the dipolar contrast of the stripes reverses as well. In the case of the medium disks, the contrast once again indicates a curling of the magnetization. With respect to the crosses, similar to the FeCu system, a different behavior for the magnetization reversal can be inferred from the difference in contrast intensity along the long and short branches.

4. Conclusions

In this work, electrodeposition of complex FeCu and FePd geometric structures onto pre-lithographed substrates was demonstrated, which opens new possibilities from the viewpoint of materials and applications beyond permalloy, probably the most utilized Fe alloy in electrodeposited structures so far. The fabricated features show different growth patterns and microstructures as a result of the dissimilar electrolyte formulations. While compositionally-graded structures are obtained for the FeCu system with a 60 at% Fe content in the center region, compositionally homogeneous $Fe_{62}Pd_{38}$ motifs are obtained for the FePd system. In any case, fast deposition rates (3.5 s for FeCu and 200 s for FePd) enable the growth of the submicron structure arrays from electrolyte formulations at a moderate pH. X-ray diffraction and SEM analyses suggest that the size of the cavities in which the structures are grown induces microstructural variations most notably in the grain size and the degree of alloying. The magnetization reversal process at room temperature for the in-plane direction of the field is

similar for the two systems and dominated by the shape anisotropy of the structures while evidence of magnetic curling is unveiled for the circular and cross-shaped structures. Moreover, the straightforward preparation technique and ferromagnetism makes them attractive candidates for a slew of prospective applications in spintronics, microelectromechanical systems and biomedicine (once these structures would be detached from the substrate).

Acknowledgements

This work was supported by the SELECTA (No. 642642) H2020-MSCA-ITN-2014 project**.** Partial financial support by the Spanish Government [Project MAT2017-86357- C3-1-R and associated FEDER], the Generalitat de Catalunya (2017-SGR-292) and the European Research Council (SPIN-PORICS 2014-Consolidator Grant, Agreement nº 648454) is acknowledged. We thank Helmholtz-Zentrum Berlin (HBZ) for the allocation of synchrotron radiation beamtime. Nanofacility Piemonte is acknowledged.

References

(1) Grünberg, P. A. Nobel Lecture: From spin waves to giant magnetoresistance and beyond. *Rev. Mod. Phys.* **2008**, *80*, 1531.

(2) Stamps, R. L.; Breitkreutz, S.; Åkerman, J.; Chumak, A. V.; Otani, Y.; Bauer, G. E.; Thiele, J. U.; Bowen, M.; Majetich, S. A.; Kläui, M.; Prejbeanu, I. L.; Dieny, B.; Dempsey, N. M.; Hillebrands, B. The 2014 Magnetism Roadmap. *J. Phys. D: Appl. Phys.* **2014**, *47*, 333001.

(3) Hoffmann, A.; Bader, S. D. Opportunities at the Frontiers of Spintronics. *Phys. Rev. Appl.* **2015**, *4*, 047001.

(4) Makarov, D.; Melzer, M.; Karnaushenko, D.; Schmidt, O. G. Shapeable magnetoelectronics. *Appl. Phys. Rev.* **2016**, *3*, 011101.

(5) Lara, A.; Moreno, J. R.; Guslienko, K. Y.; Aliev, F. G. Information processing in patterned magnetic nanostructures with edge spin waves. *Sci. Rep.* **2017**, *7*, 5597.

(6) Braun, H. B. Topological effects in nanomagnetism: from superparamagnetism to chiral quantum solitons. *Adv. Phys.* **2012**, *61*, 1.

(7) Gilbert, D. A.; Maranville, B. B.; Balk, A. L.; Kirby, B. J.; Fischer, P.; Pierce, D. T.; Unguris, J.; Borchers, J. A.; Liu, K. Realization of ground-state artificial skyrmion lattices at room temperature. *Nat. Comm.* **2015**, *6*, 8462.

(8) Park, J. H.; Park, C.; Jeong, T.; Moneck, M. T.; Nufer, N. T.; Zhue, J.-G. Co/Pt multilayer based magnetic tunnel junctions using perpendicular magnetic anisotropy. *J. Appl. Phys.* **2008**, *103*, 07A917.

(9) Mizunuma, K.; Ikeda, S.; Park, J. H.; Yamamoto, H.; Gan, H.; Hasegawa, H.; Hayakawa, J.; Matsukura, F.; Ohno, H. MgO barrier-perpendicular magnetic tunnel junctions with CoFe/Pd multilayers and ferromagnetic insertion layers, *Appl. Phys. Lett.* **2009**, *95*, 232516.

(10) Kim, G.; Sakuraba, Y.; Oogane, M.; Ando, Y.; Miyazaki, T. Tunneling magnetoresistance of magnetic tunnel junctions using perpendicular magnetization $L1_0$-CoPt electrodes. *Appl. Phys. Lett.* **2008**, *92*, 172502.

(11) Fernández-Pacheco, A.; Streubel, R.; Fruchart, O.; Hertel, R.; Fischer, P.; Cowburn, R. P. Three-dimensional nanomagnetism. *Nat. Commun.* **2017** *8*, 15756.

(12) Pfau, B.; Günther, C. M.; Hauet, T.; Eisebitt, S.; Hellwig, O. Thermally induced magnetic switching in bit-patterned media. *J. Appl. Phys.* **2017**, *122*, 043907.

(13) Chérif, S. M.; Hennequin, J. F. Submicron structures in thin layers by electron beam lithography and ion beam sputtering. J. Magn. Magn. Mater. **1997**, *165*, 504.

(14) Lau, J. W.; McMichael, R. D.; Chung, S. H.; Rantschler, J. O.; Parekh, V.; Litvinov, D. Microstructural origin of switching field distribution in patterned Co/Pd multilayer nanodots. *Appl. Phys. Lett.* **2008**, *92*, 012506.

(15) Ivanov, Y. P.; Chuvilin, A.; Vivas, L. G.; Kosel, J.; Chubykalo-Fesenko, O.; Vázquez, M. Single crystalline cylindrical nanowires – toward dense 3D arrays of magnetic vortices. *Sci. Rep.* **2016** *6*, 23844.

(16) Ivanov, Y. P.; Chuvilin, A.; Lopatin, S.; Kosel, J. Modulated Magnetic Nanowires for Controlling Domain Wall Motion: Toward 3D Magnetic Memories. *ACS Nano* **2016**, *10*, 5326.

(17) Arshad, M. S.; Šturm, S.; Zavašnik, J.; Espejo, A. P.; Escrig, J.; Komelj, M.; McGuiness, P. J.; Kobe, S.; Rožman, K. Ž. Effect of magnetocrystalline anisotropy on the magnetic properties of electrodeposited Co-Pt nanowires. *J. Nanoparticle Res.* **2014**, *16*, 2688.

(18) Dislaki, E.; Sort, J.; Pellicer, E. Parametric aqueous electrodeposition study and characterization of Fe–Cu films. *Electrochim. Acta* **2017**, *231*, 739.

(19) Dislaki, E.; Robbennolt, S.; Campoy-Quiles, M.; Nogués, J.; Pellicer, E.; Sort, J. Coercivity Modulation in Fe–Cu Pseudo-Ordered Porous Thin Films Controlled by an Applied

Voltage: A Sustainable, Energy-Efficient Approach to Magnetoelectrically Driven Materials. *Adv. Sci.* **2018**, 5, 1800499.

(20) Chien, C. L.; Liou, S.; Kofalt, D.; Yu, W.; Egami, T.; Watson, T. J.; McGuire, T. R. Magnetic properties of Fe_xCu_{100-x} solid solutions. *Phys. Rev. B* **1986**, *33*, 3247.

(21) Hong, I. T.; Koo, C. H. Antibacterial properties, corrosion resistance and mechanical properties of Cu-modified SUS 304 stainless steel. *Mat. Sci. Eng. A* **2005**, *393*, 213.

(22) Konczak, C.; Haehnel, V.; Schultz, L.; Schlörb, H. *Mater. Chem. Phys.* **2016** *174*, 150.

(23) Pérez-Landazábal, J. I.; Lambri, O. A.; Bonifacich, F. G.; Sánchez-Alarcos, V.; Recarte, V.; Tarditti, F. Influence of defects on the irreversible phase transition in Fe–Pd ferromagnetic shape memory alloys. *Acta Mater.* **2015**, *86* , 110.

(24) Cui, J.; Shield, T. W.; James, R. D. Phase transformation and magnetic anisotropy of an iron–palladium ferromagnetic shape-memory alloy. *Acta Mater.* **2004**, *52*, 35-47.

(25) Kauffmann-Weiss, S.; Hamann, S.; Gruner, M. E.; Buschbeck, J.; Ludwig, A.; Schultz, L. S. Fähler, Understanding the Magnetic Shape Memory System Fe–Pd–X by Thin Film Experiments and First Principle Calculations. *Adv. Eng. Mater.* **2012**, *14*, 724.

(26) Morley, S. A.; Riley, S. T.; Porro, J.-M.; Rosamond, M. C.; Edmund, H.; Cunningham, J. E.; Langridge, S.; Marrows, C. H. Effect of FePd Alloy Composition on the Dynamics of Artificial Spin Ice. *Sci. Rep.* **2018**, *8*, 4750.

(27) Sapozhnikov, M. V.; Ermolaeva, O. L. Two-dimensional skyrmion lattice in a nanopatterned magnetic film. *Phys. Rev. B* **2015**, *91*, 024418.

(28) Jasen, P. V.; Gonzalez, E. A.; Castellani, N. J.; Juan, A. Theoretical study of hydrogen adsorption on FePd face-centered cubic alloy surfaces. *Phys. Rev. B* **2005**, *71*, 235422.

(29) Bryden, K. J.; Ying, J. Y. Pulsed Electrodeposition Synthesis and Hydrogen Absorption Properties of Nanostructured Palladium‐Iron Alloy Films. *J. Electrochem. Soc.* **1998**, *145*, 3339.

(30) Huang, Y. X.; Liu, X. W.; Sun, X. F.; Sheng, G. P.; Zhang, Y. Y.; Yan, G. M.; Wang, S. G.; Xu, A. W.; Yu, H. Q. A new cathodic electrode deposit with palladium nanoparticles for cost-effective hydrogen production in a microbial electrolysis cell. *Int. J. Hydrog. Energy* **2011**, *36*, 2773.

(31) Cardoso, J. A. S. B.; Amaral, L.; Metin, Ö.; Cardoso, D. S. P.; Sevim, M.; Sener, T.; Sequeira, C. A. C.; Santos, D. M. F. Reduced graphene oxide assembled Pd-based nanoalloys for hydrogen evolution reaction. *Int. J. Hydrog. Energy* **2017**, *42*, 3916.

(32) Zink, M.; Mayr, S. G. Ferromagnetic shape memory alloys: synthesis, characterisation and biocompatibility of Fe–Pd for mechanical coupling to cells. *Mater. Sci. Technol.* **2014**, *30*, 1579.

(33) Kim, D. H.; Rozhkova, E. A.; Ulasov, I. V.; Bader, S. D.; Rajh, T.; Lesniak, M. S.; Novosad, V. Biofunctionalized magnetic-vortex microdiscs for targeted cancer-cell destruction. *Nat. Mater.* **2010**, *9*, 165.

(34) Rozhkova, E.A.; Novosad, V.; Kim, D.H.; Pearson, J.; Divan, R.; Rajh, T.; Bader, S.D. Ferromagnetic microdisks as carriers for biomedical applications. *J. Appl. Phys.* **2009**, *105*, 07B306.

(35) Baumgärtner, M. E.; Gabe, D. R. Palladium-Iron Alloy Electrodeposition. Part II Alloy Plating Systems. *Trans. IMF* **2000**, *78*, 79.

(36) Rožman, K. Ž.; Pečko, D.; Šturm, S.; Maver, U.; Nadrah, P.; Bele, M.; Kobe, S. Electrochemical synthesis and characterization of $Fe_{70}Pd_{30}$ nanotubes for drug-delivery applications. *Mater. Chem. Phys.* **2012** *133*, 218.

(37) Többens, D. M.; Zander, S. KMC-2: an X-ray beamline with dedicated diffraction and XAS endstations at BESSY II. *JLSRF* **2016**, *2*, 49.

(38) Wojdyr, M. Fityk: a general-purpose peak fitting program. *J. Appl. Crystallogr.* **2010**, *43* 1126.

(39) Xie, Q.; Hong, M. H.; Tan, H. L.; Chen, G. X.; Shi, L. P.; Chong, T. C. Fabrication of nanostructures with laser interference lithography. *J. Alloy Compd* **2008**, *449*, 261.

(40) Varea, A.; Pané, S.; Gerstl, S.; Zeeshan, M. A.; Özkale, B.; Nelson, B. J.; Suriñach, S.; Baró, M. D.; Nogués, J.; Sort, J.; Pellicer, E. Ordered arrays of ferromagnetic, compositionally-graded $Cu_{1-x}Ni_x$ alloy nanopillars prepared by template-assisted electrodeposition. *J. Mater. Chem. C* **2013** *1*, 7215.

(41) Neykova, N.; Hruska, K.; Holovsky, J.; Remes, Z.; Vanecek, M. Arrays of ZnO nanocolumns for 3-dimensional very thin amorphous and microcrystalline silicon solar cells. *Thin Solid Films* **2013**, *543*, 110.

(42) Quintana, A.; Varea, A.; Guerrero, M.; Suriñach, S.; Baró, M. D.; Sort, J.; Pellicer, E. Structurally and mechanically tunable molybdenum oxide films and patterned nanostructures by electrodeposition. *Electrochim. Acta* **2015**, *173*, 705.

(43) Gómez, E.; Pellicer, E.; Vallés, E. Microstructures of soft-magnetic cobalt–molybdenum alloy obtained by electrodeposition on seed layer/silicon substrates. *Electrochem. Commun.* **2004**, *6*, 853.

(44) Luo, J. K.; Chu, D.; Flewitt, A. J.; Spearing, S. M.; Fleck, N. A.; Milne, W. I. Uniformity Control of Ni Thin-Film Microstructures Deposited by Through-Mask Plating. *J. Electrochem. Soc.* **2005**, *152*, C36.

(45) Turchanin, M. A.; Agraval, P. G.; Nikolaenko, I. V. Thermodynamics of alloys and phase equilibria in the copper-iron system. *J. Phase Equilib.* **2003** *24*, 307.

(46) Zha, C. L.; Dumas, R. K.; Fang, Y. Y.; Bonanni, V.; Nogués, J.; Åkerman, J. Continuously graded anisotropy in single $(Fe_{53}Pt_{47})_{100-x}Cu_x$ films *J. Appl. Phys. Lett.* **2010**, *97*, 182504.

(47) Kirby, B. J.; Davies, J. E.; Liu, K.; Watson, S. M.; Zimanyi, G. T.; Shull, R. D.; Kienzle, P. A.; Borchers, J. A. Vertically graded anisotropy in Co/Pd multilayers. *Phys. Rev. B* **2010**, *81*, 100405.

(48) Varaprasad, B. C. S.; Wang, J.; Shiroyama, T.; Takahashi, Y. K.; Hono, K. Columnar Structure in FePt–C Granular Media for Heat-Assisted Magnetic Recording. *IEEE Trans. Magn.* **2015**, *51*, 3200904.

(49) Boom, R.; De Boer, F. R.; Niessen, A. K.; Miedema, A. R. Enthalpies of formation of liquid and solid binary alloys based on 3d metals: III. Alloys of iron. *Physica B+C* **1983**, *115*, 285.

(50) Porter, D. A.; Easterling, K. E.; Sherif, M. *Transformations in Metals and Alloys, (Revised Reprint)* CRC press, **2009**.

(51) Ghosh, G.; Kantner, C.; Olson, G. B. Thermodynamic modeling of the Pd-X (X=Ag, Co, Fe, Ni) systems. *J. Phase Equilib.* **1999**, *20*, 295.

(52) Bajaj, S.; Haverty, M. G.; Arróyave, R.; Shankar, S. Phase stability in nanoscale material systems: extension from bulk phase diagrams. *Nanoscale* **2015**, *7*, 9868.

(53) Ross, C. A.; Hwang, M.; Shima, M.; Cheng, J. Y.; Farhoud, M.; Savas, T. A.; Smith, H. I.; Schwarzacher, W.; Ross, F. M.; Redjdal, M.; Humphrey, F. B. Micromagnetic behavior of electrodeposited cylinder arrays. *Phys. Rev. B* **2002**, *65*, 144417.

(54) Pribiag, V. S.; Krivorotov, I. N.; Fuchs, G. D.; Braganca, P. M.; Ozatay, O.; Sankey, J. C.; Ralph, D. C.; Buhrman, R. A. Magnetic vortex oscillator driven by d.c. spin-polarized current. *Nat. Phys.* **2007**, *3*, 498.

Figure captions

Figure 1. SEM micrographs of FeCu electrodeposited arrays of a) stripes, b) disks and c) crosses in three distinct sizes (increasing from left to right).

Figure 2. SEM micrographs of the nine FePd arrays of a) stripes, b) disks and c) crosses in three sizes (increasing from left to right).

Figure 3. AFM images of the a) large-sized FeCu and b) medium-sized FePd disks, crosses and stripes.

Figure 4. STEM bright field images of the a) FeCu and b) FePd lamellae.

Figure 5. a) Indexed SAED pattern taken at a middle point of the FeCu medium-sized cross, b) HR-TEM image, c) EDX/STEM compositional maps and d) EELS mixed elemental map.

Figure 6. a) SAED pattern taken at a middle point in the FePd medium-sized cross b) HR-TEM micrograph, c) bright field image of sample and d) EELS mixed compositional map.

Figure 7. X-ray diffractograms obtained from the FeCu and FePd medium-sized dots.

Figure 8. MFM images of the FeCu structures taken a,e) under a static field of 600 Oe, b,f) at remanence after removal of the field as well as c,g) and d,h) following the same steps upon reversal of the field direction.

Figure 9. Hysteresis loops measured in-plane for the FeCu large single-feature arrays of the a) large disks, b) small disks and c) medium-sized crosses along the long axis.

Figure 10. MFM images of medium-sized FePd motifs a) under a static field of 400 Oe, b) at remanence and c,d) following the same steps upon reversal of the applied field direction.

Table 1. Detailed dimensions of the nine arrays of patterned structures.

Geometry	Dimensions		
	Small	**Medium**	**Large**
Stripes	150 nm x 450 nm	300 nm x 900 nm	450 nm x 1.35 μm
Disks	d: 200 nm	d: 500 nm	d: 1 μm
Crosses	300 nm x 500 nm	600 nm x 1 μm	900 nm x 1.5 μm

Table 2. Average height and RMS surface roughness values for the nine arrays of FeCu patterned structures as determined by AFM.

FeCu structures			
Geometry	**Dimensions**		
	Small	**Medium**	**Large**
Stripes	–	RMS = 23 Z_{avg} = (180 ± 6) nm	RMS = 23 Z_{avg} = (168 ± 10) nm
Disks	RMS = 23 nm Z_{avg} = (187 ± 13) nm	RMS = 18 Z_{avg} = (188 ± 4) nm	RMS = 24 Z_{avg} = (189 ± 3) nm
Crosses	RMS = 19 Z_{avg} = (209 ± 5) nm	RMS = 16 Z_{avg} = (212 ± 15) nm	RMS = 12 Z_{avg} = (209 ± 18) nm

Table 3. Average height and RMS surface roughness values for the nine arrays of FePd patterned structures as determined by AFM.

FePd structures			
Geometry	**Dimensions**		
	Small	**Medium**	**Large**
Stripes	RMS = 9 Z_{avg} = (112 ± 2) nm	RMS = 14 Z_{avg} = (215 ± 7) nm	RMS = 20 Z_{avg} = (214 ± 15) nm
Disks	RMS = 10 nm Z_{avg} = (145 ± 2) nm	RMS = 6 Z_{avg} = (166 ± 3) nm	RMS = 15 Z_{avg} = (140 ± 2) nm
Crosses	RMS = 10 Z_{avg} = (188 ± 1) nm	RMS = 16 Z_{avg} = (180 ± 6) nm	RMS = 21 Z_{avg} = (196 ± 7) nm

Table 4. Values of 2θ position, d-spacing and lattice constant for the FeCu crosses of different dimensions.

Size	FeCu crosses		
	2θ [º]	**d [Å]**	**Lattice constant [Å]**
Large	44.41 ± 0.07	2.064 ± 0.002	2.918 ± 0.002
Medium	44.44 ± 0.03	2.062 ± 0.002	2.917 ± 0.002
Small	44.45 ± 0.02	2.062 ± 0.002	2.916 ± 0.002

Table 5. Values of 2θ position, d-spacing and lattice constant for the FePd crosses of different dimensions.

Size	FePd crosses		
	2θ [º]	**d [Å]**	**Lattice constant [Å]**
Large	43.09 ± 0.03	2.124 ± 0.003	2.994 ± 0.003
Medium	43.25 ± 0.01	2.116 ± 0.001	2.993 ± 0.001
Small	43.24 ± 0.01	2.118 ± 0.001	3.005 ± 0.001

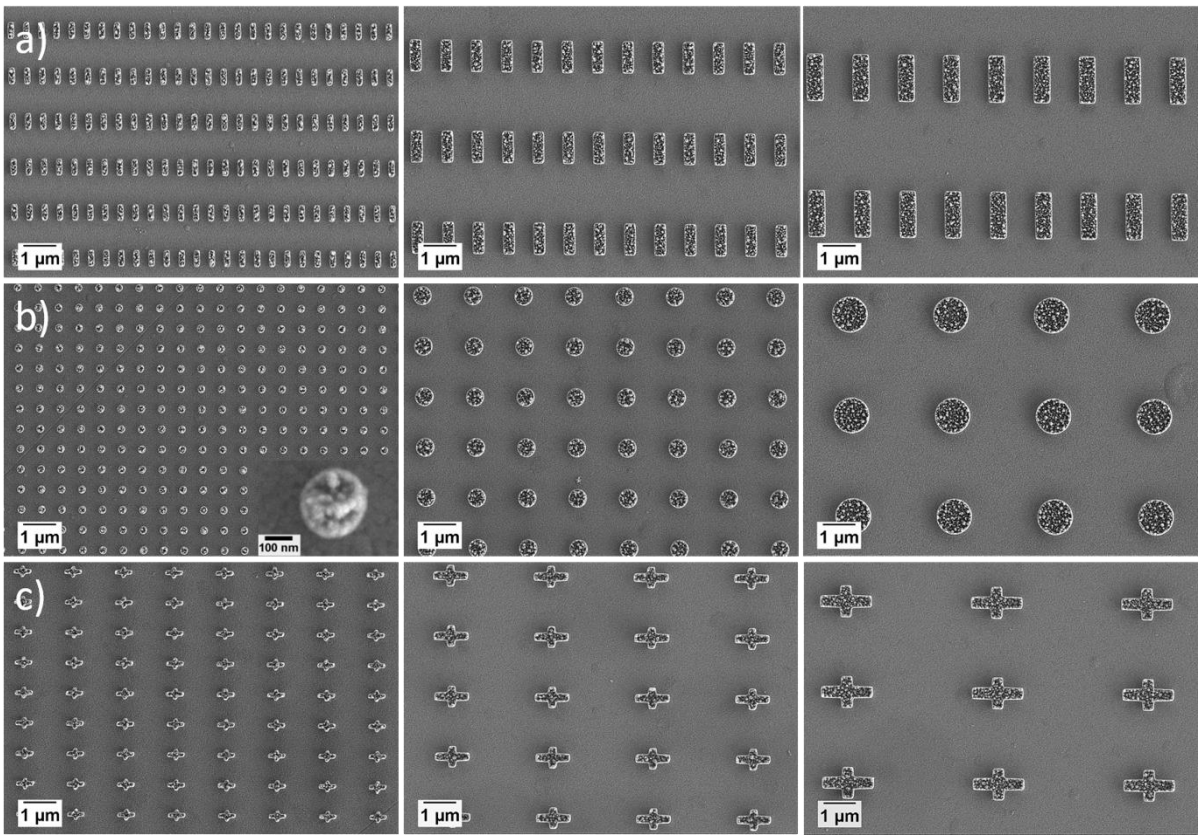

Figure 1

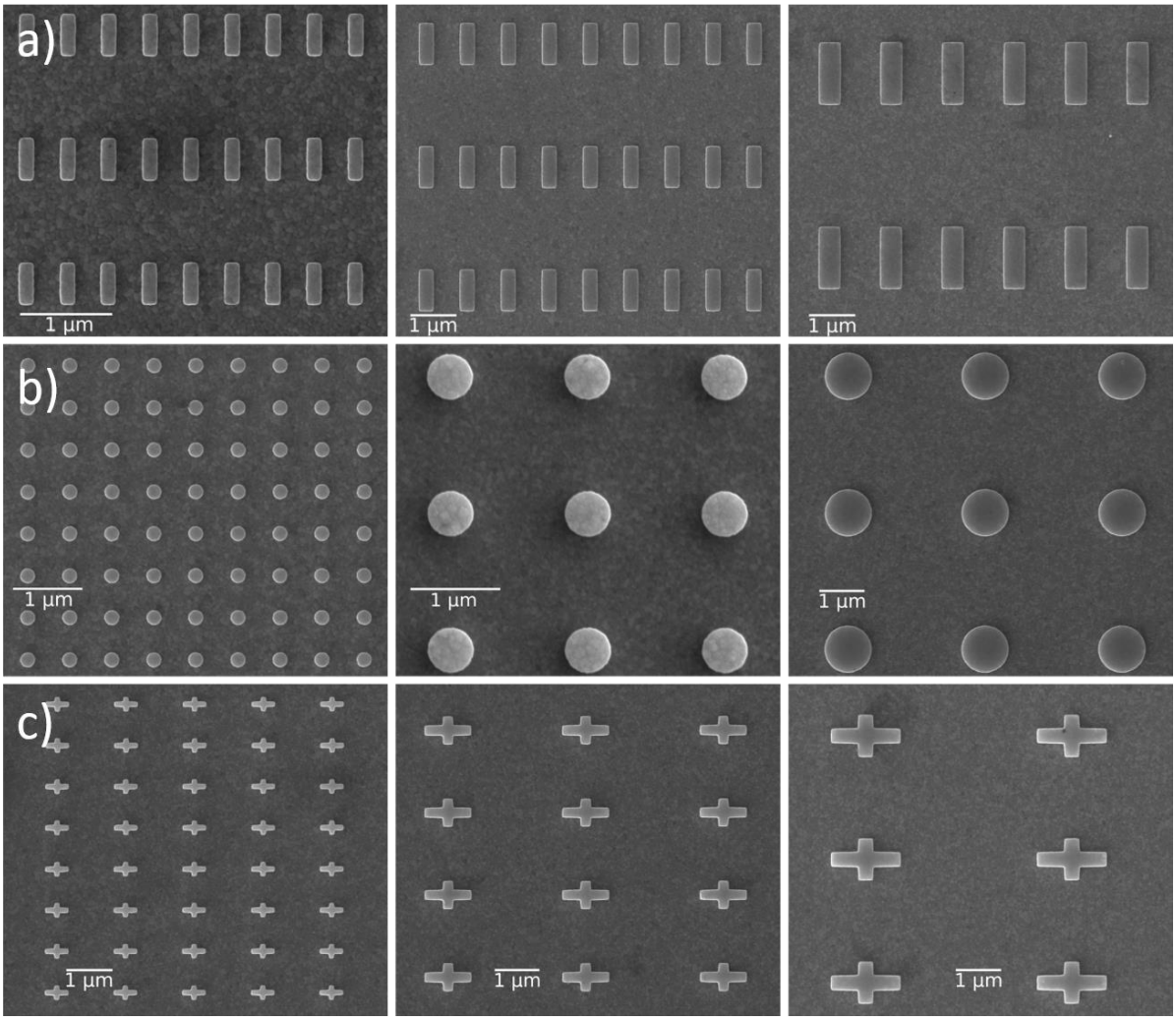

Figure 2

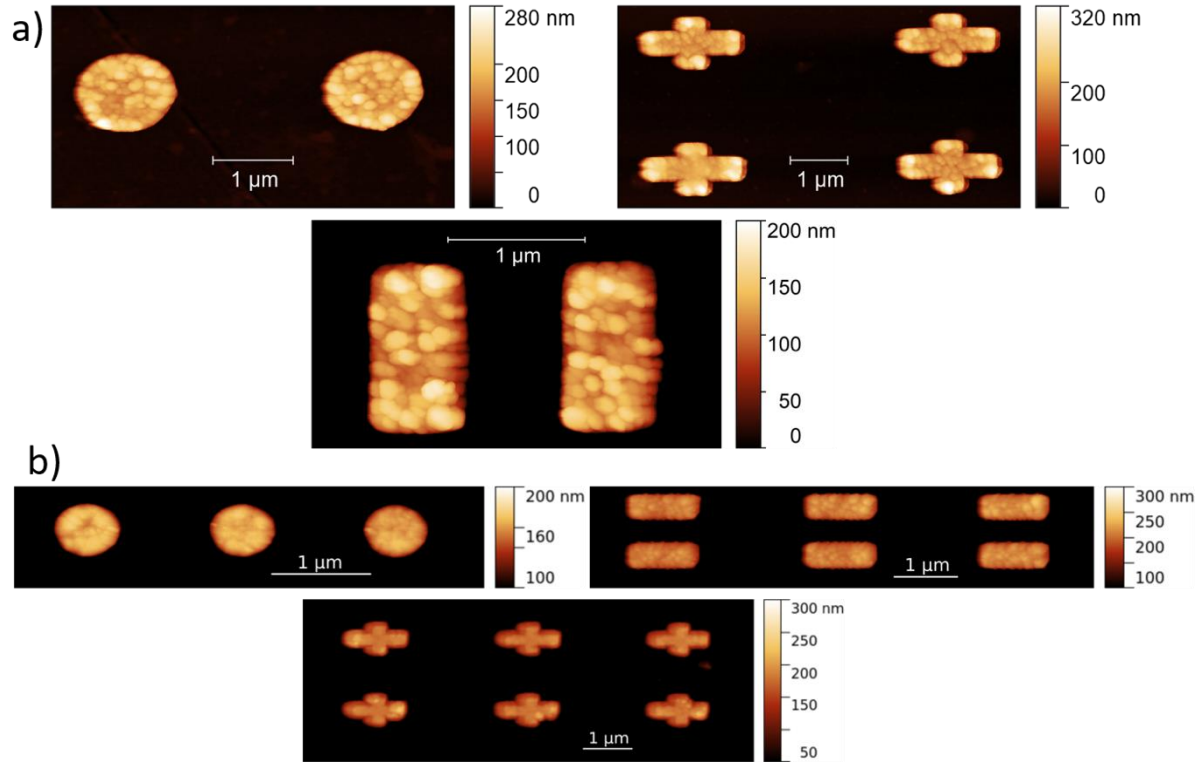
a)
1 µm
280 nm
200
150
100
0
1 µm
320 nm
200
100
0
1 µm
200 nm
150
100
50
0
b)
1 µm
200 nm
160
100
1 µm
300 nm
250
200
100
1 µm
300 nm
250
200
150
50

Figure 3

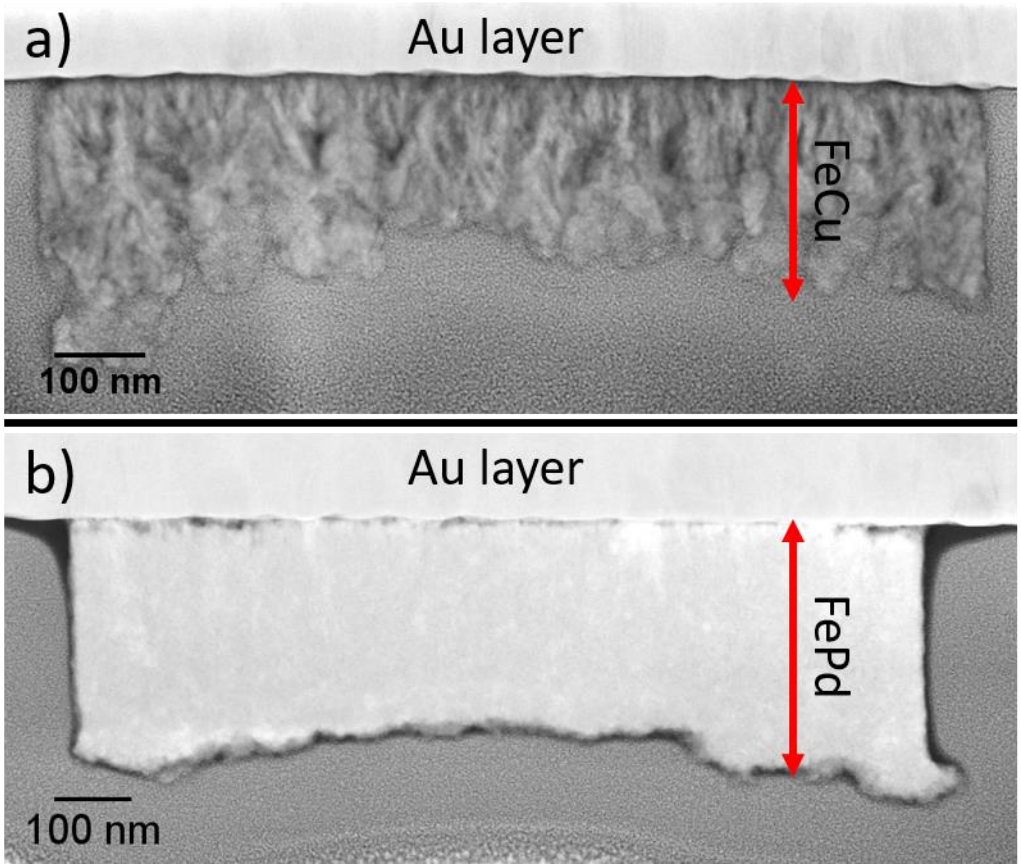

Figure 4

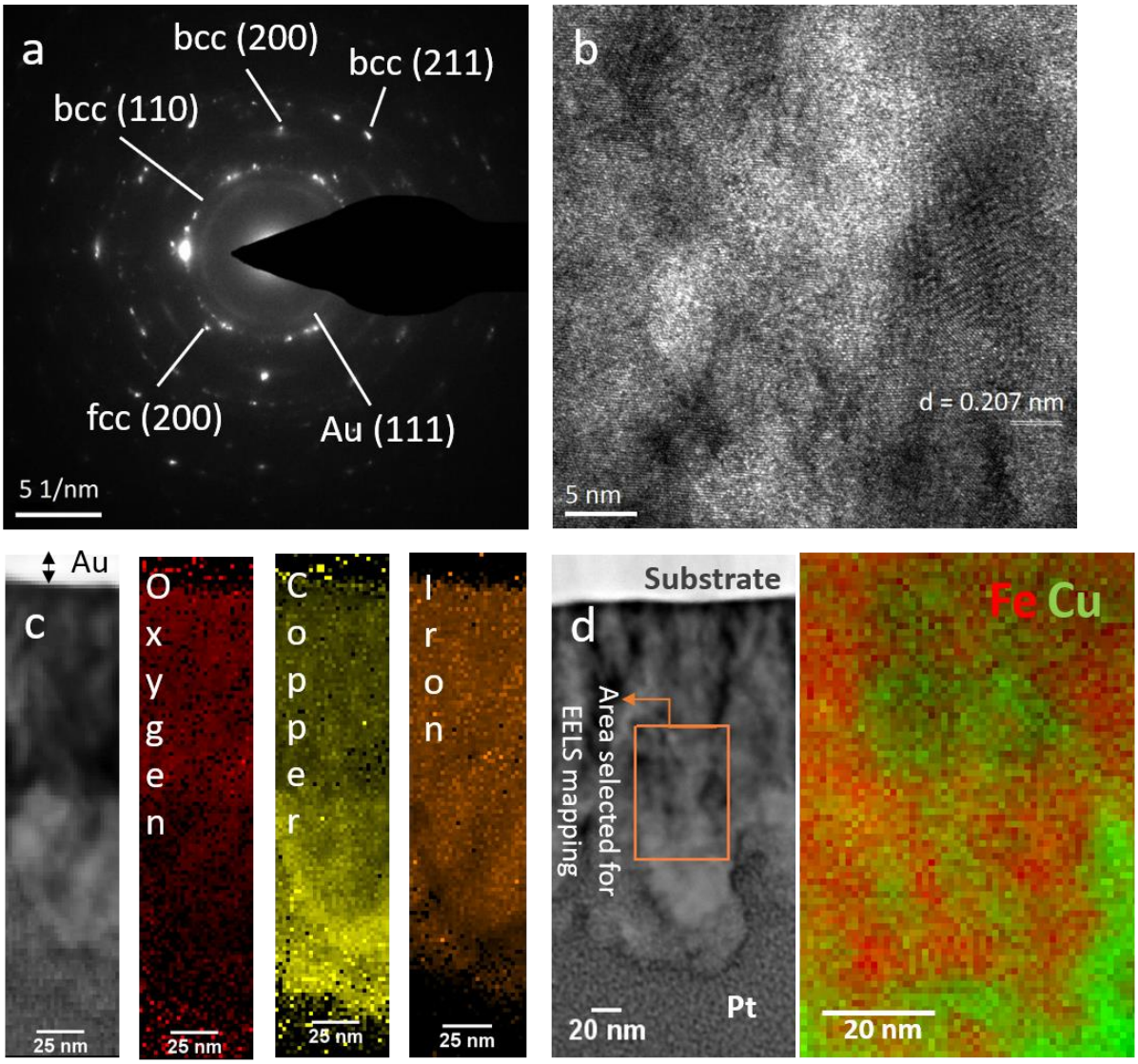
a
bcc (200)
bcc (211)
bcc (110)
fcc (200)
Au (111)
5 1/nm
b
d = 0.207 nm
5 nm
Au
c
25 nm
Oxygen
25 nm
Copper
25 nm
Iron
25 nm
Substrate
d
Area selected for EELS mapping
Pt
20 nm
Fe Cu
20 nm

Figure 5

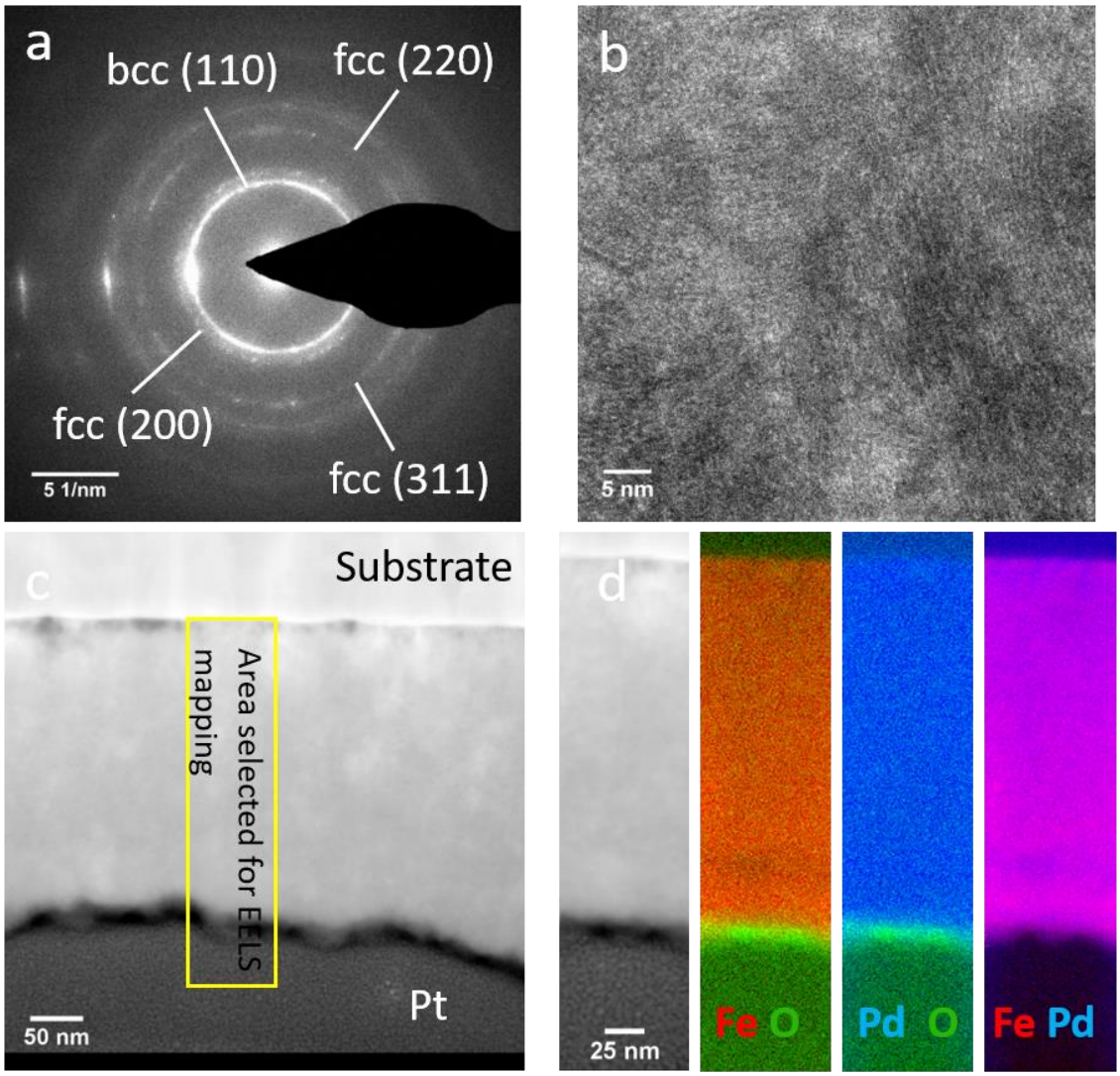
a
bcc (110)
fcc (220)
fcc (200)
fcc (311)
5 1/nm
b
5 nm
c
Substrate
Area selected for EELS mapping
Pt
50 nm
d
25 nm
Fe O
Pd O
Fe Pd

Figure 6

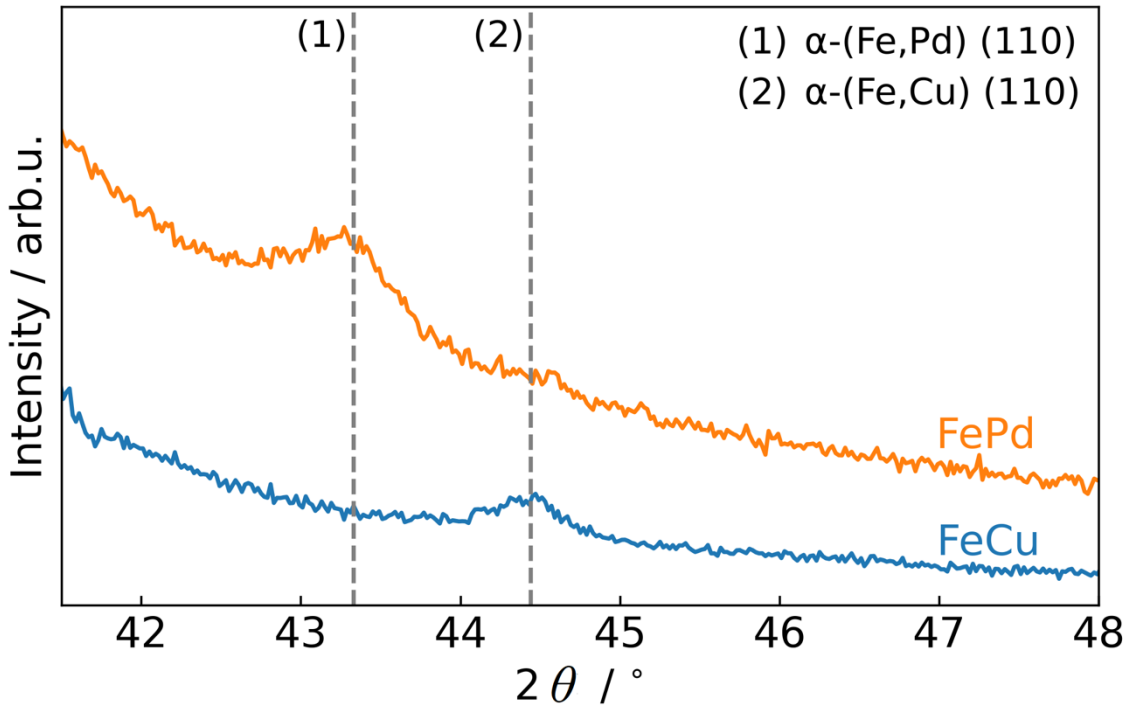
(1)
(2)
(1) α-(Fe,Pd) (110)
(2) α-(Fe,Cu) (110)
FePd
FeCu
Intensity / arb.u.
42
43
44
45
46
47
48
2θ / °

Figure 7

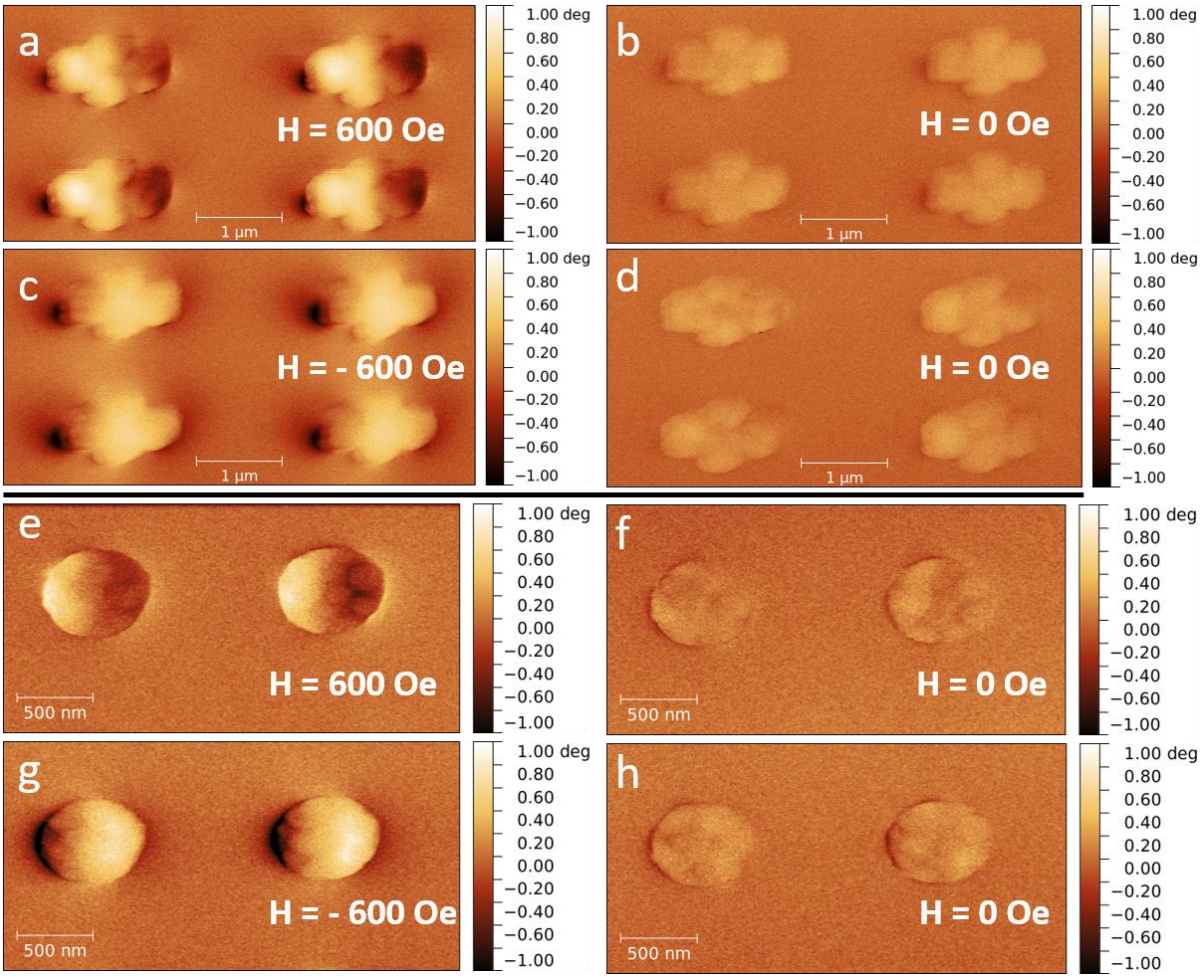
a
H = 600 Oe
1 µm
b
H = 0 Oe
1 µm
c
H = - 600 Oe
1 µm
d
H = 0 Oe
1 µm
e
H = 600 Oe
500 nm
f
H = 0 Oe
500 nm
g
H = - 600 Oe
500 nm
h
H = 0 Oe
500 nm
1.00 deg
0.80
0.60
0.40
0.20
0.00
−0.20
−0.40
−0.60
−1.00

Figure 8

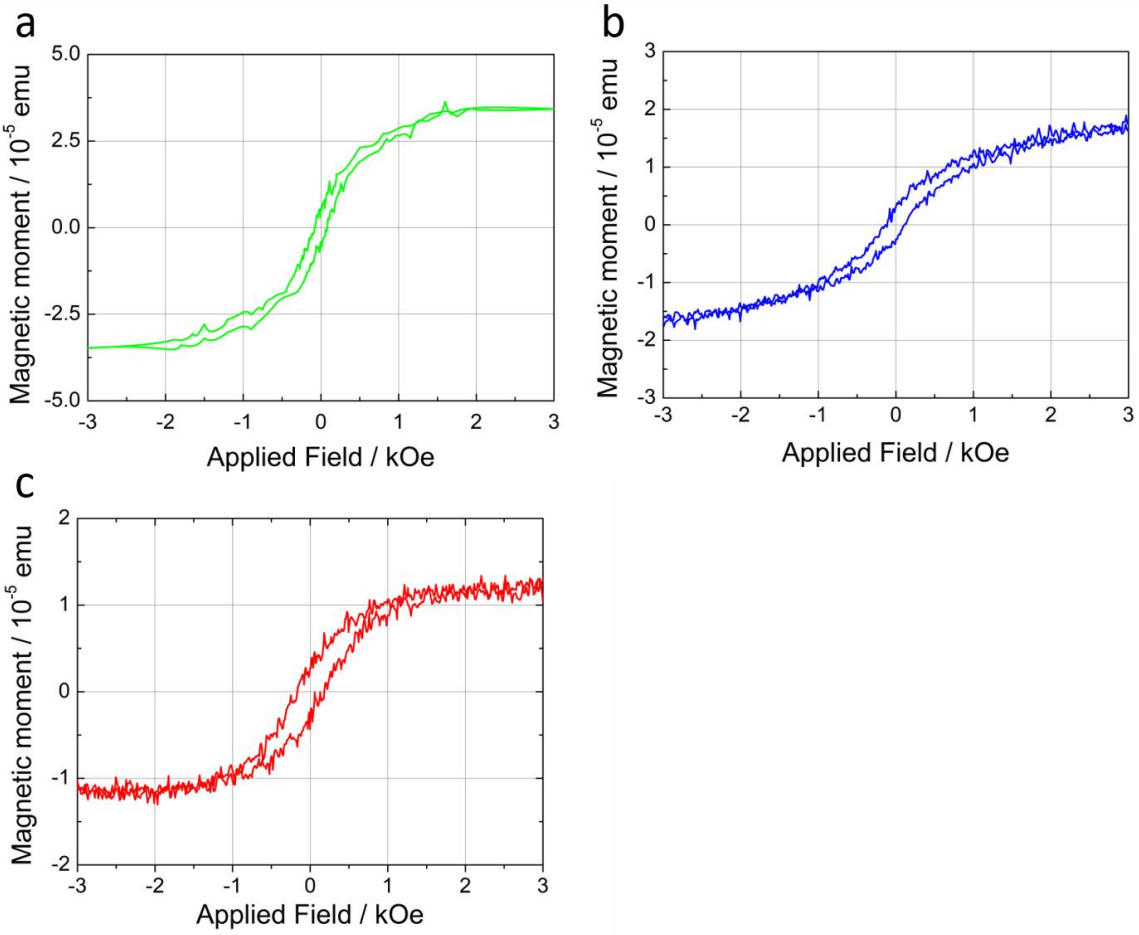
a
Magnetic moment / 10-5 emu
5.0
2.5
0.0
-2.5
-5.0
-3
-2
-1
0
1
2
3
Applied Field / kOe
b
Magnetic moment / 10-5 emu
3
2
1
0
-1
-2
-3
-3
-2
-1
0
1
2
3
Applied Field / kOe
c
Magnetic moment / 10-5 emu
2
1
0
-1
-2
-3
-2
-1
0
1
2
3
Applied Field / kOe

Figure 9

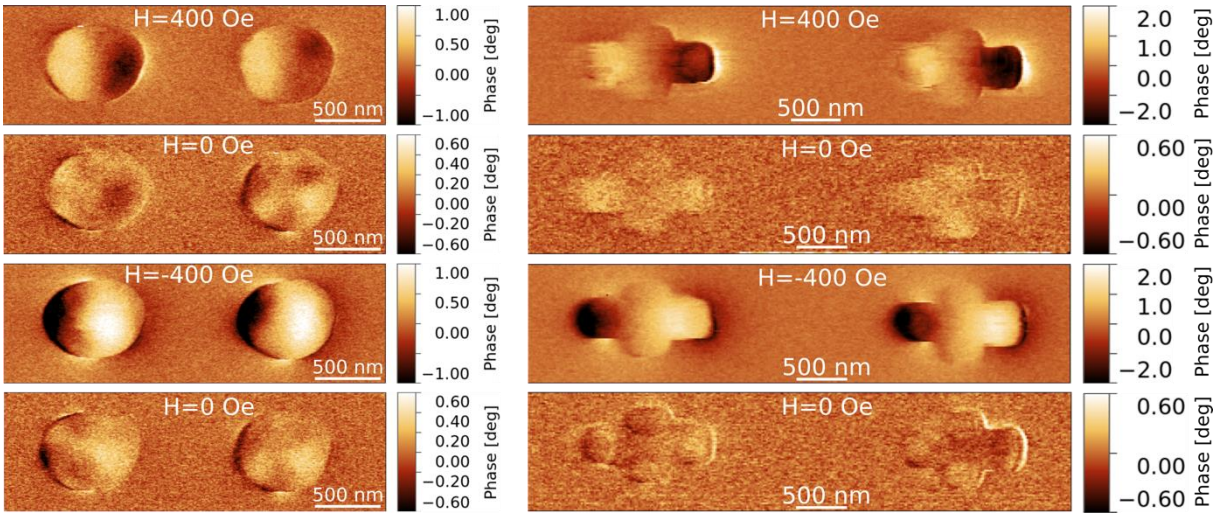
H=400 Oe
500 nm
1.00
0.50
0.00
−1.00
Phase [deg]
H=0 Oe
500 nm
0.60
0.40
0.20
0.00
−0.20
−0.60
Phase [deg]
H=-400 Oe
500 nm
1.00
0.50
0.00
−1.00
Phase [deg]
H=0 Oe
500 nm
0.60
0.40
0.20
0.00
−0.20
−0.60
Phase [deg]
H=400 Oe
500 nm
2.0
1.0
0.0
−2.0
Phase [deg]
H=0 Oe
500 nm
0.60
0.00
−0.60
Phase [deg]
H=-400 Oe
500 nm
2.0
1.0
0.0
−2.0
Phase [deg]
H=0 Oe
500 nm
0.60
0.00
−0.60
Phase [deg]

Figure 10